Journal of Energy Storage 54 (2022) 105218

Contents lists available at ScienceDirect

Journal of Energy Storage

journal homepage: www.elsevier.com/locate/est

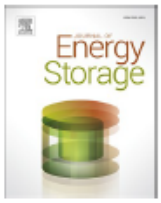

Research Papers

Simulated discharge overpotential distributions for sintered electrode batteries in rechargeable coin cell form factors

Chen Cai, Donovan Hensley, Gary M. Koenig Jr. *

Department of Chemical Engineering, University of Virginia, 102 Engineers Way, Charlottesville 22904-4741, VA, USA

ARTICLE INFO

Keywords:
Simulation
Thick electrode
Lithium-ion battery
Small form factor rechargeable

ABSTRACT

Sintered electrode lithium-ion batteries contain only electroactive material which has undergone a mild thermal treatment to improve particle connectivity and thus electrode mechanical strength. These electrodes can be made very thick, and due to the lack of inactive binders or conductive additives there are ion transport advantages relative to equivalent thickness and porosity composite electrodes. In this study, the discharge of sintered electrode full cells was simulated at the cell level for three different form factors: CR2032, CR2025, and CR2016. Simulations also include relatively high and low rates of discharge and two different electrolytes. Using the simulations, overpotential distributions enable analysis of the contributors to resistance in the cell analyzed for the different regions of the anode, cathode, and separator. Overpotential sources include electronic overpotential, ionic overpotential, interfacial overpotential, and OCV overpotential. As the total thickness increases, the main overpotential contribution shifts from interfacial to ionic, with both originating from the electrodes. In all cases a higher conductivity electrolyte dramatically increases total capacity delivered at higher discharge rates.

1. Introduction

Rechargeable lithium-ion batteries (LIBs) have become the predominant power source for portable electronics and electric vehicles [1]. Research has pursued improving both the volumetric and gravimetric energy densities of LIB cells, not only through new materials but also via electrode and cell engineering [2–7]. As one example, increasing the thickness of a LIB electrode significantly improved the areal energy density, but ionic transport limitations became more severe at high cycling rates/current densities [6,8,9]. Ionic transport limitations due to tortuous interstitial regions in the electrode were generated from the electrode microstructure and can be exacerbated by materials and processing including polymer binders, conductive additives, and electrode calendaring [9–11]. In order to reduce these transport limitations at increased thickness, electrodes free of inactive materials have been pursued. These include "sintered electrodes" comprised of only electroactive LIB materials which undergo a mild sintering step to improve mechanical properties of the porous ceramic thin film [5–8]. Such electrode design and processing avoided the use of spatially obstructive polymer binder and conductive carbon, resulting in reduced ionic transport restrictions (e.g., the Bruggeman exponent for sintered electrodes has been reported to achieve the hard sphere ideal limit of 1.5, while composite electrodes with inactive materials have been reported to exceed 3) [6,8,10]. Sintered electrodes have been reported with high thicknesses over 500 μm and areal loadings on the order of hundreds of mg cm^{-2} [4–8,12,13].

However, due to thicknesses much greater than typical composite electrodes, ion transport in the electrolyte phase through the interstitial microstructure of the solid sintered electrodes still resulted in high polarization which limited rate capability [4,6,8]. It is noted that various approaches have been pursued to mitigate this limitation, including modifying the electrode microstructure to facilitate improved ion transport and/or implementing higher conductivity electrolytes [4,12,14–19]. Understanding the capabilities of sintered electrode full cells for a set form factor can have additional value. In this work, numerical simulation of the electrochemical properties of sintered electrode structures representative of thicknesses to maximize capacity for a series of coin cell form factors (CR2032, CR2025, CR2016) will be described, as well as the different contributors to the electrode polarization. For these simulations, the anode and cathode was limited to $Li_4Ti_5O_{12}$ and $LiCoO_2$ that has been used in previous reports [5–8,18,19], although other material substitutions are possible [12,20].

* Corresponding author at: Department of Chemical Engineering, University of Virginia, 102 Engineers' Way, P.O. Box 400741, Charlottesville, VA 22904, USA.
E-mail address: gary.koenig@virginia.edu (G.M. Koenig).

https://doi.org/10.1016/j.est.2022.105218
Received 9 April 2022; Received in revised form 25 May 2022; Accepted 24 June 2022
Available online 6 July 2022
2352-152X/© 2022 Elsevier Ltd. All rights reserved.

The coin cell form factors in this work were chosen for direct comparison with existing cells that have these established form factors commercially. While not as large of a market for LIB as applications such as electric vehicles and mobile phones, rechargeable small form factor cells have been suggested for many emerging applications such as wearable electronics [21]. The framework provided in this work can be extended more generally to planar electrodes with a variety of geometries, where thick electrodes would be desirable to increase cell level energy density. The coin cell geometry was chosen for direct comparison to existing commercial coin cell technology and because experimentally coin cells have been used by researchers as a form factor to evaluate high energy density electrodes and cells [5,22].

2. Methods

The simulation framework was based on Newman's pseudo-two dimensional (P2D) system [23,24], but incorporated variable electronic conductivity of both cathode ($Li_{1-x}CoO_2$) and anode ($Li_{4+3y}Ti_5O_{12}$) as a function of lithiation [8]. The system of partial differential equations (PDEs) has been reported in previous publications [8], and is provided in the Supporting information as well. The total thickness of both cathode and anode in each cell type were chosen to maximize available electrochemical energy within constraints of the materials of construction for the different form factors. The thicknesses for inactive components were based on measured thicknesses for commercial materials. These included one top piece (250 μm thick), one bottom piece (250 μm), one spacer (500 μm), one spring and one glass fiber separator (together 200 μm after assumed compression for both components). It is noted that some of these values can be varied with different cell materials/fabrication, that the use of wave spring and glass fiber separator makes the total thickness (due to varying compression) variable, and that the spacer could be thinner. However, all values were typical for commercial coin cell parts used in previous sintered electrode cells fabricated and reported in prior studies [6–8,18,19]. The total remaining combined thicknesses available for both electrodes were then determined to be approximately 2000 μm for CR2032, 1300 μm for CR2025, and 400 μm for CR2016. The individual cathode and anode thicknesses were determined by calculating the practical theoretical maximum capacity. The results were a ratio of 45 % cathode and 55 % anode with an area of 2 cm^2 (based on the inner diameter of −1.6 cm for CR2032 gasket), based on the pore/void volume fraction and theoretical capacity for cathode assumed to be 0.4 and 137 mAh g^{-1} and for anode assumed to be 0.4 and 175 mAh g^{-1} [8]. The calculated theoretical capacity for increments of 5 % variation of thickness/volume fraction for the anode and cathode can be found in Supporting information, Fig. S1.

Detailed electrode simulation parameters are listed in Table 1. Two electrolytes considered in this work were 1.2 M $LiPF_6$ in 3:7 ethylene carbonate:ethyl methyl carbonate (referred to herein as "Gen2") and 2.0 M lithium bis(fluorosulfonyl)imide (LiFSI) in dimethyl carbonate, with detailed parameters listed in Table 2. Gen2 was chosen as a common battery electrolyte formulation, and the LiFSI electrolyte was considered due to its higher conductivity, which would be expected to mitigate the ionic transport resistances experienced in thick sintered electrodes [19]. Other relevant simulation parameters can be found in Table 3.

To calculate the overpotential distribution, a transmission line model (Fig. 1) was used. When discharging a battery, current passes via solid electrode (with electronic resistance) or liquid electrolyte (with ionic resistance). The bridge between solid electrode and liquid electrolyte is where the electrochemical reaction occurs (with interfacial resistance). Due to the different extents of lithiation at the surface of the solid electrode at different particles and electrode depths, the open circuit voltages can vary across the electrode thickness during discharge (resulting in open circuit voltage, or OCV, differences). Thus, there are numerous current paths, the quantity of which is equal to the number of discretized points used in the P2D simulation. In the simulations in this study, there are 50 discretized thickness locations each for the cathode and anode for all cases. In this parallel circuit model, according to Kirchoff's law, any current path has the same voltage drop, but current density (a sum of currents traverse via solid electrode and via liquid electrolyte per conservation of charge) across each path could vary due to the balancing of the 4 resistances mentioned above. In other words, the current density across each path is the Li^+ intercalation or

Table 1
Electrode parameters used in simulations.

Parameters	Cathode value	Anode value
Solid state Li^+ diffusivity (m^2 s^{-1})	3.5×10^{-13} [25]	2.0×10^{-12} [26]
Active material radius (m)	2×10^{-7} [27]	1.7×10^{-7} [28]
Porosity	0.4 [6,8]	0.4 [6,8]
Bruggeman exponent	1.5 [8]	1.5 [8]
Rate constant ($m^{2.5}$ $mol^{-0.5}$ s^{-1})	3.10×10^{-13} [29]	3.90×10^{-13} [30]
Density (kg m^{-3})	5010 [31]	3480 [32]
Capacity (mAh g^{-1})	274 [33]	175 [33]
Variable conductivity (S m^{-1})	$7000 \times (1-x)^2 + 5 \times (1-x) + 0.054$, $0.5 \le x \le 1.0$ in Li_xCoO_2 [34,35]	$Exp(4.37 \times (1-y)^{200}) \times 300 \times (y + 10^{-6})^{0.38} \times 5^{(y-1)}$, $0 \le y \le 1.0$ in $Li_{4+3y}Ti_5O_{12}$ [37]
Open circuit voltage (V)	$-(Tanh((x - 0.555) \times 5.7) - 1) / 3.1 - (Exp(59(x - 0.84)) + 1) / 4000 + (Tanh(6.2(x - 0.73)) - 1) / 45 + Exp(-(x - 0.5) \times 400) / 40 + 3.895$, $0.5 \le x \le 1.0$ in Li_xCoO_2 [8,36]	$0.20946 \times Exp(-y / 0.00855) + 0.45108 \times Exp(-5000y) + 0.27706 \times Exp(-1010.1y) + 1.544 - Exp(50(y - 0.87)) \times 0.001$, $0 \le y \le 1.0$ in $Li_{4+3y}Ti_5O_{12}$ [8]

Table 2
Electrolyte parameters used in simulations.

Electrolyte and other parameters	$LiPF_6$ value	LiFSI value
Transference number, t_+^0	0.415 [38]	0.65 [17]
Initial concentration (mol m^{-3})	1200 [19]	2000 [19]
Thermodynamic factor $\left(1 + \frac{\partial ln f_\pm}{\partial ln c}\right)(1 - t_+^0)$	$0.28687\,c^2 + 0.74678\,c + 0.44103$ [39]	0.35, assuming $\frac{\partial ln f_\pm}{\partial ln c}$ is 0
Conductivity (S m^{-1})	$0.1297c^3 + 2.51c^{1.5} + 3.329c$ [39]	$0.28 \times c^2 + 0.54 \times c$, $c \le 1$; $0.06 \times c^3 - 0.58 \times c^2 + 1.51 \times c - 0.17$, $1 < c \le 4$; $22.432 \times Exp(-0.989 \times c)$, $c > 4$ [15,16]
Diffusivity (m^2 s^{-1})	$6.7185 \times Exp(-1.081 \times c) / (0.812 \times Exp(-0.381 \times c) \times 10^{-10}$ [39]	$2.7941 \times Exp(-0.892 \times c)$ [16]

Table 3
Separator and other parameters used in simulations.

Separator and other parameters	Value
Temperature (K)	298.15, room temperature
Gas constant (J K^{-1} mol^{-1})	8.3145
Faraday constant (A s mol^{-1})	96,485
Separator thickness (μm)	200, assumed based on cell geometry
Separator MacMullin number [40]	1.84, experimental
Separator porosity	0.95, assumed based on cell geometry and manufacturer specifications

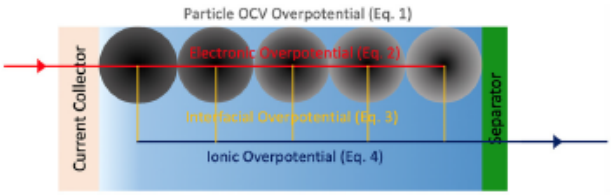

Fig. 1. Cartoon illustrating the overpotential contributions and distribution across one electrode, with only five nodes shown to simplify the illustration.

deintercalation rate at each position.

Thus, to calculate the overpotential/resistance at a certain location of an electrode:

$$\varphi_{OCV}(n) = \mathrm{OCV}\left(c_s^{surface}(n)\right) - \mathrm{OCV}\left(c_s^{surface}(0)\right) \quad (1)$$

$$\varphi_{electronic}(n) = \phi_1(n) - \phi_1(0) \quad (2)$$

$$\varphi_{interfacial}(n) = \phi_1(n) - \phi_2(n) - \mathrm{OCV}\left(c_s^{surface}(n)\right) \quad (3)$$

$$\varphi_{ionic}(n) = \phi_2(n) - \phi_2(0)) \quad (4)$$

where $c_s^{surface}$, φ_1, φ_2, and n represent electrode solid phase surface Li^+ concentration, solid electrode potential, liquid electrolyte potential, and nth discretized point. Then, to calculate the current-weighted overpotential contribution of the cell during discharge the total intercalation or deintercalation rate (which is constant due to the galvanostatic operation of the cell, the total charge or discharge current) is normalized by:

$$\eta_{OCV} = \sum_{n=0}^{N} \frac{j(n)}{j_{total}} (\varphi_{OCV}(n)) \quad (5)$$

$$\eta_{electronic} = \sum_{n=0}^{N} \frac{j(n)}{j_{total}} (\varphi_{electronic}(n)) \quad (6)$$

$$\eta_{interfacial} = \sum_{n=0}^{N} \frac{j(n)}{j_{total}} (\varphi_{interfacial}(n)) \quad (7)$$

$$\eta_{ionic} = \sum_{n=0}^{N} \frac{j(n)}{j_{total}} (\varphi_{ionic}(n)) \quad (8)$$

$$\eta_{\%} = \frac{\eta_{OCV}(any\ other\ type)}{\eta_{OCV} + \eta_{electronic} + \eta_{interfacial} + \eta_{ionic}} \times 100\% \quad (9)$$

where j represents Li^+ intercalation/deintercalation rate and N is the total number of discretized points. Eqs. (1)–(9) above were not extracted from a specific prior work. They resulted from application of previously established transmission line models and Kirchoff's law to the planar electrode P2D system simulation results [40–45].

3. Results & discussions

3.1. Rate capability simulations

The simulated discharge capacities of the three different form factor cells as a function of total discharge current are shown in Fig. 2. The data in Fig. 2 on a log-log scale can be found in Supporting information, Fig. S2. Note that in all cases the geometric electrode areas were 2 cm^2, thus for comparison to current density the currents can be divided by a factor of 2. Also, for all simulations the initial lithiation state was 0.50 and 0.92 for all locations within the cathode and anode, respectively (e.g., corresponding to a uniform "fully charged" state). The assumptions to obtaining such values were that LCO could only accommodate 50 % delithiation to prevent structural collapse [46–50], and the LTO was

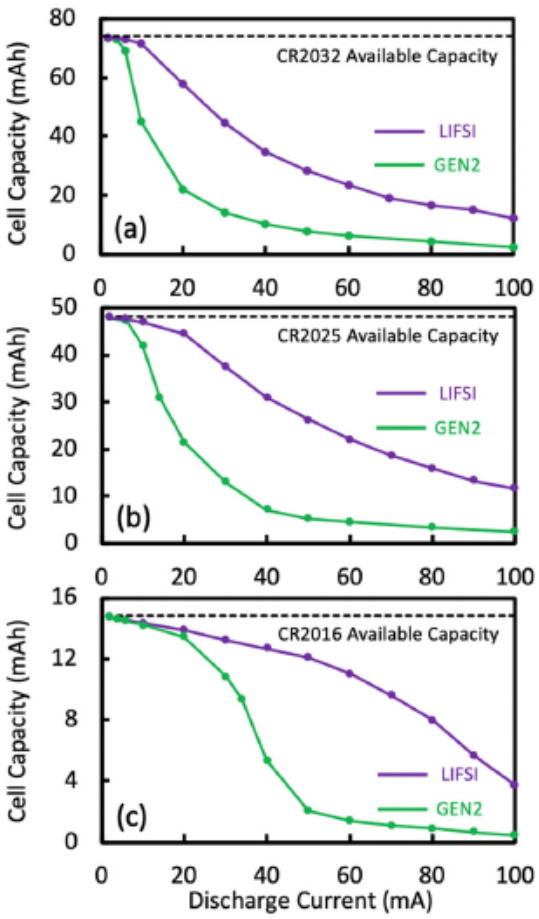

Fig. 2. Simulated discharge capacity as a function of discharge current for LTO/LCO sintered electrodes starting from the fully charged state. The form factors simulated were (a) CR2032, (b) CR2025, and (c) CR2016 for the cases where the electrolytes were either Gen2 (green circles) or LiFSI-based (purple circles). Lines have been added to guide the eye. Assumed electrode geometric areas were 2 cm^2. (For interpretation of the references to color in this figure legend, the reader is referred to the web version of this article.)

then correspondingly calculated from conservation of charge and the capacity assumed available in the LTO.

The CR2032 form factor had the greatest capacity available due to the highest total thickness and thus most total electroactive material within the cell. At low rate (2 mA) for both electrolytes simulated, the discharge capacity approached the theoretical capacity available in the cell (74 mAh), with the Gen2 and LiFSI electrolyte both achieving 73 mAh. The Gen2 electrolyte cell had a sharp decrease in discharge capacity with increasing rate (Fig. 2a), where at 20 mA the capacity dropped to 20 mAh (27 % retention) and at 50 mA the discharge capacity dropped down to 8 mAh (11 % retention). However, with LiFSI, the capacity drop was reduced at increasing rates and correspondingly the discharge capacity was 58 mAh at 20 mA (78 % retention) and 28 mAh (39 % retention) at 50 mA. For the CR2025 (Fig. 2b) and CR2016 (Fig. 2c) form factors, the general trends followed that of CR2032 with decreasing capacity at increasing rates and improved retention with the LiFSI electrolyte relative to the Gen2 electrolyte, although as the total cell/electrode thickness was decreased the total capacity delivered at low rate also decreased. For all discharge simulations, the discharge capacity at the lowest rate nearly matched that of the theoretical cell capacity. The improved capacity retention at increasing rates for the higher conductivity LiFSI electrolyte relative to the Gen2 electrolyte, and for thinner relative to thicker electrodes, was consistent with the ion transport in the electrolyte being the process that limited the rate

capability of the sintered electrode full cells. This outcome was experimentally supported in recent reports [19,51], and will be analyzed in further detail below.

3.2. Overpotential distributions

Before discussion of specific form factors and discharge rates, an explanation for the information in Figs. 3, 4, and Supporting information, Fig. S3 is elaborated here to aid in interpretation of the data. Each figure is composed of 3 columns (a-c) and each column has four panels (the rows).

The top panel represents the discharge voltage (bottom curve at lowest voltage) with each individual current-weighted overpotential contribution shown above the simulated discharge curve. Thus, after all of the overpotentials were added the top line (highest voltage) represents uniform lithiation/delithiation of the active materials in the electrode in the absence of any overpotential contributions. In Fig. 3a, many of the overpotential contributions are difficult to differentiate in the discharge curve because they are relatively small. However, in Fig. 3b the different overpotential contributions from the different electrode regions can be differentiated in the plot. The brackets separate the overpotential contributions arising from the regions of the anode (top region), separator (middle region), and cathode (bottom regions), with brackets and text indicting the different regions. For both anode and cathode regions, blue, yellow, grey, and red represent ionic, interfacial, OCV, and electronic overpotential contributions, respectively. Green color represents the separator overpotential even though it also only contributes ionic overpotential, to better differentiate/separate the cathode and anode regions.

The second panel contains the current-weighted overpotential contributions at the end of discharge plotted as a donut chart, where the letters in the donut hole represent the overpotential origin (C, A, and S for cathode, anode, and separator, respectively) and the same color scheme was used for the types of overpotential on the donut as the discharge plot in the first row. The calculation of percentage contributions was using Eq. (9). The donut chart is specifically shown for end of

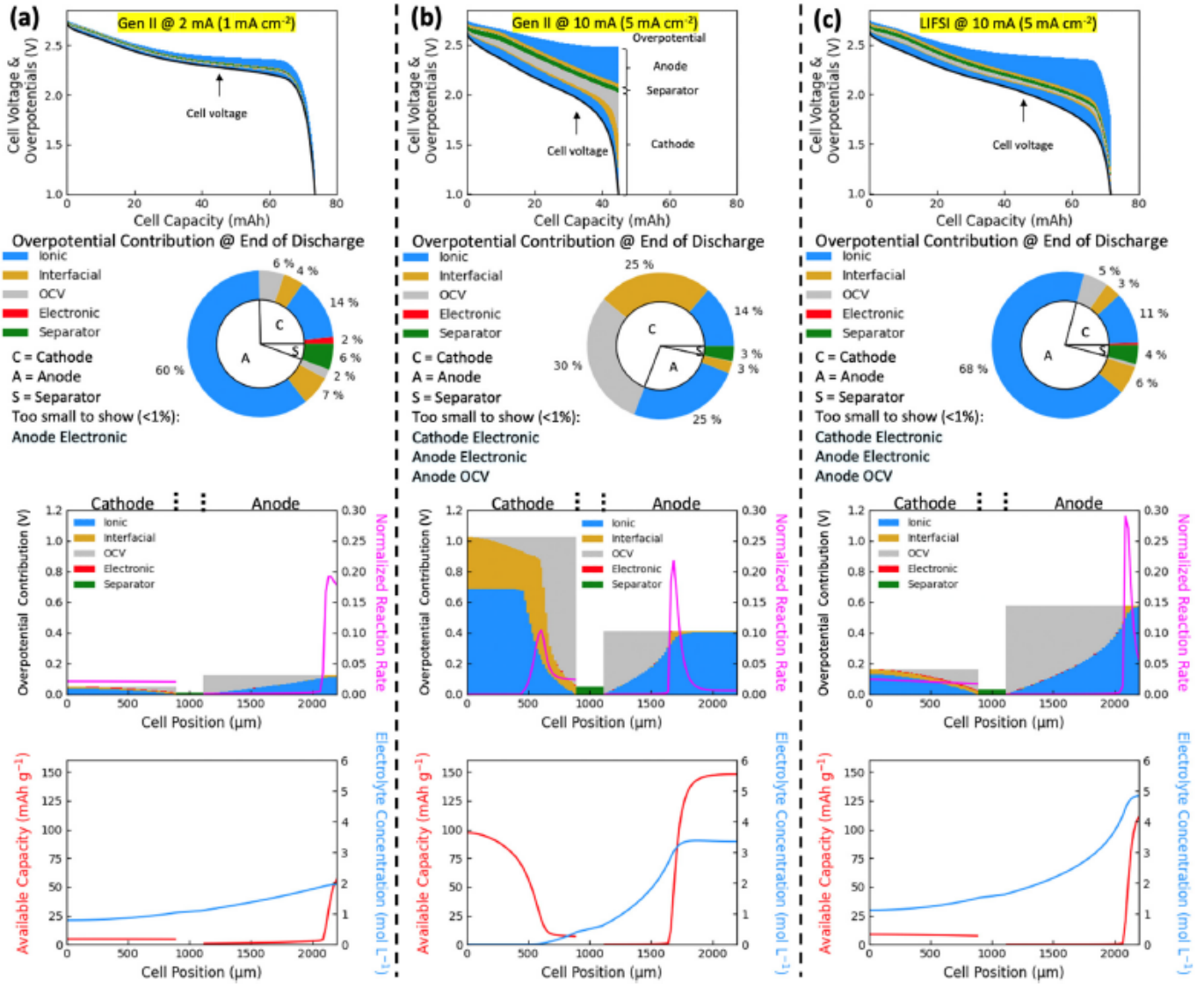

Fig. 3. Discharge simulation of CR2032 at (a) 2 mA with Gen II, (b) 10 mA with Gen II, and (c) 10 mA with LiFSI. Each column has four panels/rows showing simulated cell voltage and current weighted overpotentials (top panel), current weighted overpotential distribution at the end of discharge (second panel), position dependent electrochemical reaction distribution (pink line) and overpotential distribution at the end of discharge (third panel), and available electrode capacity (red line) & electrolyte concentration (blue line) at the end of discharge (bottom panel). Overpotential distributions correspond to the color scales as indicated on the legend, with separate components for the cathode, anode, and separator. (For interpretation of the references to color in this figure legend, the reader is referred to the web version of this article.)

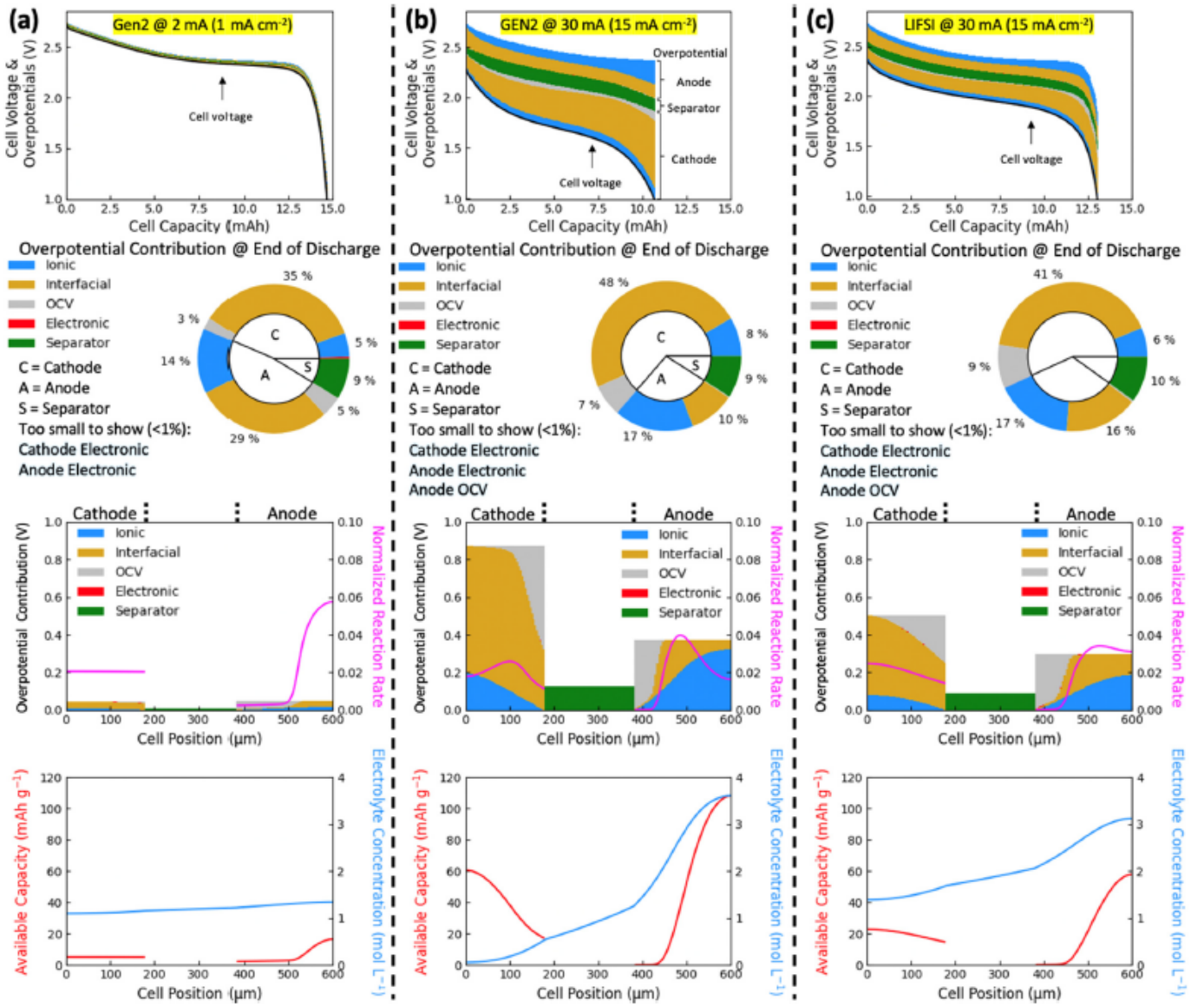

Fig. 4. Discharge simulation of CR2016 at (a) 2 mA with Gen II, (b) 30 mA with Gen II, and (c) 30 mA with LiFSI. Each column has four panels/rows showing simulated cell voltage and current weighted overpotentials (top panel), current weighted overpotential distribution at the end of discharge (second panel), position dependent electrochemical reaction distribution (pink line) and overpotential distribution at the end of discharge (third panel), and available electrode capacity (red line) & electrolyte concentration (blue line) at the end of discharge (bottom panel). Overpotential distributions correspond to the color scales as indicated on the legend, with separate components for the cathode, anode, and separator. (For interpretation of the references to color in this figure legend, the reader is referred to the web version of this article.)

discharge as this is when the overpotential is the greatest and provides insights into the factors most limiting extracting additional capacity from the cell, if additional capacity is still available.

The third row shows the overpotential contribution of each type and electrochemical rate distribution across the whole cell thickness at the end of discharge, where the left region is the cathode (e.g., lowest "cell position" values, where "0" corresponds to the cathode current collector), the middle is the separator, and the right is the anode (e.g., higher "cell position" values, where the maximum value corresponds to the location of the anode current collector). The total height for the overpotential contributions (values corresponding to left y-axis) of each region within each electrode has the same height according to Kirkoff's law and the transmission line model. The color scheme is the same as for the previous rows, and at each position of the cell, the relative length of each color represents the overpotential contribution from each type at each position/discretized point (Eqs. (1)–(4)). The pink curve represents the normalized electrochemical reaction rate, or lithium intercalation/deintercalation rate at each of the cathode and anode at the end of discharge (values correspond to the right y-axis). It is noted here that the second row in the plot is obtained by combining the overpotential contributions with the electrochemical reaction rate.

The bottom panel depicted the spatial profiles of available capacity remaining in the electrode (red, meaning the delithiated portion for cathode and lithiated portion for anode; values correspond to left y-axis) and electrolyte concentration (blue, values correspond to right y-axis) across the battery at the end of discharge as a function of depth with the same location convention as in the third row.

3.3. Overpotential analysis

Simulation analysis for CR2032, the thickest cell, can be found in Fig. 3 for the cell discharged at 2 mA with Gen2 electrolyte (Fig. 3a), 10 mA with Gen2 electrolyte (Fig. 3b), and 10 mA with LiFSI electrolyte (Fig. 3c). When the cell was discharged at a relatively low rate of 2 mA

(Fig. 2a), nearly all the available capacity was delivered, and the total overpotential was small with a maximum of −0.1 V at 60 mAh discharged capacity. In looking at the overpotential distribution at the end of discharge, it can be seen that 60 % of the overpotential originated from the ionic resistance in the anode. The information in the third row of Fig. 3a provided further insights into this overpotential. Even though the electrolyte concentration gradient was relatively mild across the cell thickness, at the end of discharge in the anode region the electrochemical reaction was concentrated near the current collector region. This was because there was minimal available capacity left in the anode regions near the separator. As a result, a large portion of the current had to be carried by the electrolyte phase, creating a large ionic resistance in the anode region. However, in the cathode region, not only the electrochemical reaction but available capacity was much more homogenously distributed even at the end of discharge. To aid in understanding this phenomenon, dynamic videos of the panels in Fig. 3a during the discharge process with the same organization are provided in the Supporting information, Video S1. Throughout the discharge process, the cathode maintained a relatively homogenously distributed intercalation rate as a function of depth. An exception was between 40 and 65 mAh when there was a small reaction front initiated from the separator side which propagated towards the current collector, where LCO had a flat OCV function at this lithiation state right before the end of discharge. Such phenomenon could be explained from the tendency of current passing through lowest resistance routes, where during most discharge times, the solid electrode electronic conductivity was much greater than liquid electrolyte ionic conductivity. Combining the favorable electronic transport compared to ionic transport with the flat OCV for LCO as a function of degree of lithiation at later discharge time resulted in a front that propagated due to the combination of the lowest ionic overpotential in regions closest to the separator where there was still accessible capacity. When the OCV function was not flat (e.g., LCO discharging capacity outside the 40–65 mAh portion), the OCV difference provided a driving force to smooth out the preferable ionic overpotential closer to the separator region, resulting a more homogenously distributed electrochemical reaction rate across the electrode. In contrast, throughout the discharge the anode region had a sharp reaction front which propagated from the separator towards the current collector, because LTO had a flat OCV function over nearly its full lithiation range. The observed relatively uniform LCO lithiation and LTO delithiation propagation from the separator towards the current collector was consistent with prior reports of both experiments and simulations [6–8,23,52]. In addition, the electronic overpotential was relatively small throughout the discharge and contributed only −2 % of overpotential from even the generally lower electronic conductivity cathode region for this conductive additive-free system. During most of the simulated cell conditions, for $Li_{4+3x}Ti_5O_{12}$ ($0 < x < 1$) and $Li_{1-x}CoO_2$ ($0 < x < 0.5$), the electronic conductivity for both materials used literature values of ≥ 1 S m^{-1} for over 98 % of the lithiation range [8,34,35,37]. A recent report suggested that electrode matrix electronic conductivity above this value no longer limited electrochemical capacity [11,15,16,39,53]. The electrolyte in that report had a similar ionic conductivity to this study, although it is noted the electrode thicknesses were smaller.

Starting from the same initial state, at an increased discharge rate of 10 mA only 45 mAh of capacity was delivered. Since the total overpotential was much greater than the lower current case, individual overpotential contributions were more easily recognized and labeled (Fig. 3b and Supporting information, Video S2). The ionic overpotential in the separator was much greater due to the increased current/current density. During the initial 20 mAh of discharge, over half the overpotential originated from the cathode region. After the initial 20 mAh capacity, the overpotential from the anode region continually increased as the discharge proceeded, similar to the 2 mA discharge case. Starting at 30 mAh capacity delivered, the interfacial overpotential in the cathode region became much greater, and at the end of discharge, the OCV and interfacial overpotential contributions were over 50 % of the total current-weighted overpotential (second row in Fig. 3b). On close examination of the electrolyte and electrode profile in the bottom panel, it was found that in the cathode the electrolyte was depleted near the current collector region and only about the one third of the cathode region nearest to the separator had an electrolyte concentration >0.1 M (out of 1.2 M initial concentration) and ionic conductivity >0.25 S m^{-1} (for 0.92 S m^{-1} initial ionic conductivity). This depleted electrolyte concentration/conductivity at depths further from the current collector was coupled with relatively low remaining capacity near the separator region due to the tendency for the electrochemical capacity to be extracted from the separator region first due to lower ionic overpotential, as discussed previously. As a result, the electrochemical reaction in the cathode region after 40 mAh of discharge was largely confined to the position −600–950 μm from the current collector. This reaction region confinement increased the interfacial overpotential because of the relatively low fraction of the electroactive material surface area which was accessible/participating coupled with lower Li^+ concentration near the electroactive material interfaces. The OCV overpotential also increased because much of the higher OCV remaining capacity in the electrode was near the current collector which was not accessible electrochemically due to electrolyte concentration depletion. One important item of note was that in the sintered electrode architecture the primary particle size in the simulation was <500 nm, consistent with experimental reports [5,7,8]. Thus, solid-state diffusion transport limitations were not a significant contributor to the total overpotential and were not separately displayed. For the anode side, the total overpotential compared to the case discharged at 2 mA was greater, but the overall behavior of the electrode was quite similar to the lower current case with ionic overpotential dominating and a delithiation front which propagated towards the current collector during discharge. These outcomes of direct (ionic overpotential) and indirect (electrolyte depletion due to ion transport limitations causing OCV and interfacial overpotential increases) electrolyte mass transport limitations motivated analyzing simulations for the higher ionic conductivity LiFSI-based electrolyte to compare to Gen2.

Changing to LiFSI-based electrolyte resulted in >70 mAh discharge capacity at 10 mA, which was close to the capacity for Gen2 at 2 mA (Fig. 3c and Supporting information, Video S3). It is noted that at the lower rate of 2 mA that the LiFSI electrolyte achieved nearly the same capacity (72 mAh) as at the higher rate. At the end of discharge and also throughout the majority of the discharge process, the current-weighted overpotential contribution (Fig. 3 second row) and spatial distribution (Fig. 3 third row) resembled Gen2 at the lower 2 mA discharge, where the ionic overpotential was the major contributor and the total overpotential from the anode was greater than the cathode. Examining the bottom row, depletion of electrolyte in cathode regions was not as severe in the LiFSI electrolyte, which was attributed to both the initial higher concentration of the salt and the higher conductivity of the LiFSI electrolyte [15,16,19].

For the CR2016 form factor, which had the thinnest electrodes simulated (Fig. 4 and Supporting information, Video S4), at 2 mA discharge current −15 mAh (and >99 % available capacity) was delivered and the total overpotentials were much smaller compared to the thicker CR2032 case. When looking at the current-weighted overpotentials (Fig. 4a second row) at the end of discharge, the dominating contributor at 2 mA was not ionic overpotential which contrasted with the CR2032 case. Interfacial overpotentials from both anode and cathode were responsible for over half of the total current-weighted overpotential. This reflected the reduced ionic overpotential due to greatly reduced path length for the ionic current from shorter ion transport distances in the thinner electrodes. However, because the discharge rate and geometric current density were the same, the equivalent amount of charge had to traverse a reduced electrolyte-electrode interfacial area (with less total active material). Inspection of the third row also revealed that the electrochemical reaction rate distribution in the anode was broader at the end of discharge relative to the thicker electrode CR2032

case, which was also attributed to the reduced electrode thicknesses. The bottom row of Fig. 4a shows that the electrolyte gradient was relatively small (total of −0.2 M even at end of discharge), again due to the much thinner electrodes and thus reduced ion transport limitations.

The CR2016 form factor simulation at higher discharge rate was at a higher current than the CR2032 to better understand the processes that limited rate capability, because the thinner electrodes generally can tolerate higher absolute and relative rates of discharge while delivering high fractions of available capacity compared to the thicker electrodes of the CR2032 form factor. When discharged at 30 mA with Gen2 electrolyte (Fig. 4b and Supporting information, Video S5), the cell voltage compared to that at 2 mA was lower due to the higher overpotentials. At initial stages of discharge, the overpotential contributions from the cathode were approximately of the same magnitude as from the anode. As the discharge proceeded, the cathode interfacial contribution increased due to both the decreasing electrolyte concentration in the cathode and higher lithium concentration at the particle surface (Supporting information, Eq. (S4)). The anode ionic overpotential also increased with a similar trend as the CR2032 case at 2 mA discharge as discussed above, where a reaction front propagated from the separator side towards the current collector side. At the end of discharge (Fig. 4b second row), the cathode interfacial overpotential contributed almost half of the total overpotential. Looking at the third and bottom panels, similar to analysis of the CR2032 discharge (Fig. 3b) there was high OCV overpotential due to less capacity available near the lower ionic overpotential separator region. The resistances near the current collector and separator regions resulted in a peak in the electrochemical reaction distribution in the cathode near the middle region of the electrode. Although electrolyte depletion was not as severe for the thinner electrodes in the CR2016 case, the impact of the higher conductivity LiFSI-based electrolyte was also explored for this form factor with the sintered electrode cell.

With the LiFSI electrolyte (Fig. 4c and Supporting information, Video S6), the overall voltage was much greater than that with Gen2, with an average discharge voltage of 1.940 V compared to 1.676 V. The cathode interfacial overpotential was reduced, in large part due to the greater electrolyte concentration throughout the cathode during discharge. The LiFSI concentration did not drop below 1.5 mol L^{-1} throughout the cell depth during discharge, which was due to a combination of an initially greater electrolyte concentration and the faster diffusivity and higher conductivity of LiFSI relative to Gen2. One item noted here was that the P2D model assumed the reaction rate constant did not vary with the change of electrolyte system [24,52,54,55]. However, recent reports have shown the reaction rate constant could vary [51,56]. Future work should experimentally assess this assumption if discrepancies are found with simulations.

As mentioned earlier, a CR2025 form factor cell with electrode thicknesses intermediate to the ones discussed above was also simulated. These results can be found in the Supporting information, Fig. S3 and Videos S7–S9. The CR2025 thickness resulted in more balanced contributions to the overpotential from ionic and interfacial resistance (relative to the more interfacial-dominated CR2016 and ionic-dominated CR2032). The low rate discharge (2 mA, Fig. S3a) followed what was observed for the other two form factor cells with relatively low total overpotential and −47 mAh of capacity delivered relative to the maximum available of −48 mAh. When discharged at a high rate (20 mA, between the high rate examples of 10 mA for the CR2032 and 30 mA for the CR2016) using Gen2, the depletion of Li^+ concentration within the cathode was severe, while after substitution of the LiFSI electrolyte the delivered capacity increased from −20 mAh to −44 mAh.

3.4. Further considerations

Here some limitations of the simulations in this study and future directions are discussed. As mentioned briefly earlier, the electrochemical reaction rate constant used in the Butler-Volmer equation for the simulations was independent of the electrolyte chosen. However, such assumptions might not hold true according to recent reports [51,56]. It is not expected that this assumption would have much relative impact for the thicker electrode simulations because at low rate the total overpotentials were low regardless, and at higher rates the rate limiting factor was very high overpotential resulting from ion transport limitations. However, the rate constant assumption would have a much greater impact on the simulations as the total electrode thicknesses decreased. As the electrode thickness decreased, especially for equivalent current densities or total currents at the cell level, more current must be passed through even less relative electroactive surface area. More comprehensive characterizations of the electrochemical rate constant as a function of electrolyte composition, including ion concentration which will change during the discharge process, will aid in increasing the accuracy of the simulation predictions. In addition, for the LiFSI electrolyte the transference number was assumed to be a constant due to lack of concentration-dependent data [17]. Accurately measured transference numbers as a function of concentration would further increase the model accuracy, although it is difficult to predict the impact of this assumption because it depends on the quantitative relationship between transference number and ion concentration in the electrolyte for the particular electrolyte.

4. Conclusions

This report simulated the discharge behavior of sintered electrode full cells with LTO anodes and LCO cathodes for three different form factors: CR2032, CR2025, and CR2016. The simulations were conducted at relatively high and low rates, where at the low rates nearly all the capacity was delivered and at higher rates only a fraction of the available capacity was delivered due to high overpotentials that developed within the cells at increasing rates. Detailed analysis of the individual overpotential contributions led to the conclusion that both directly and indirectly ion transport limitations were responsible for the limited capacity delivered for the thicker electrodes (e.g., CR2032 case). Simulation of a higher conductivity electrolyte resulted in much higher delivered capacity at identical rates and further supported the ion transport limitations in the cells. Two electrolytes, Gen2 and LiFSI, were compared. Rate capabilities were simulated and it was found that as the total thickness went up, the ability to retain capacity at increasing rates was negatively impacted. For thinner electrodes (e.g., CR2016 case), the ionic overpotential was less limiting and interfacial resistance became a relatively more significant consideration. Overall, this study demonstrates capacities expected for sintered electrode full cells and their relevant rate limitations, which were largely dictated by the ion transport through the electrode microstructure and electrolyte conductivity. Close inspection of the overpotential contributions also provided insights into how the reaction proceeded as a function of cell depth and the interplay of different factors on lithiation/delithiation behavior including how flat the OCV profile was for the materials and relative ionic and electronic resistances. These results provided a basis for considerations in thick sintered electrode cell design in relevant cell-level form factors.

Supplementary data to this article can be found online at https://doi.org/10.1016/j.est.2022.105218.

CRediT authorship contribution statement

Chen Cai: Conceptualization, Methodology, Investigation, Data curation, Writing – original draft.
Donovan Hensley: Methodology, Investigation.
Gary M. Koenig Jr.: Conceptualization, Resources, Writing – review & editing, Supervision, Project administration, Funding acquisition.

Declaration of competing interest

The authors declare that they have no known competing financial interests or personal relationships that could have appeared to influence the work reported in this paper.

Acknowledgement

This research was funded by the National Science Foundation, grant CMMI-1825216.

References

[1] J.B. Goodenough, K.S. Park, The Li-ion rechargeable battery: a perspective, J. Am. Chem. Soc. 135 (2013) 1167–1176, https://doi.org/10.1021/ja3091438.
[2] K.M. Abraham, Prospects and limits of energy storage in batteries, J. Phys. Chem. Lett. 6 (2015) 830–844, https://doi.org/10.1021/jz5026273.
[3] H. Dong, G.M. Koenig, Compositional control of precipitate precursors for lithium-ion battery active materials: role of solution equilibrium and precipitation rate, J. Mater. Chem. A 5 (2017) 13785–13798, https://doi.org/10.1039/c7ta03653a.
[4] B. Delattre, R. Amin, J. Sander, J. De Coninck, A.P. Tomsia, Y.-M. Chiang, Impact of pore tortuosity on electrode kinetics in lithium battery electrodes: study in directionally freeze-cast LiNi0.8Co0.15Al0.05O2 (NCA), J. Electrochem. Soc. 165 (2018) A388–A395, https://doi.org/10.1149/2.1321802jes.
[5] J.P. Robinson, J.J. Ruppert, H. Dong, G.M. Koenig, Sintered electrode full cells for high energy density lithium-ion batteries, J. Appl. Electrochem. 48 (2018) 1297–1304, https://doi.org/10.1007/s10800-018-1242-y.
[6] Z. Nie, S. Ong, D.S. Hussey, J.M. Lamanna, D.L. Jacobson, G.M. Koenig, Probing transport limitations in thick sintered battery electrodes with neutron imaging, Mol. Syst. Des. Eng. 5 (2020) 245–256, https://doi.org/10.1039/c9me00084d.
[7] Z. Nie, P. McCormack, H.Z. Bilheux, J.C. Bilheux, J.P. Robinson, J. Nanda, G. M. Koenig, Probing lithiation and delithiation of thick sintered lithium-ion battery electrodes with neutron imaging, J. Power Sources 419 (2019) 127–136, https://doi.org/10.1016/j.jpowsour.2019.02.075.
[8] C. Cai, Z. Nie, J.P. Robinson, D.S. Hussey, J.M. LaManna, D.L. Jacobson, G. M. Koenig, Thick sintered electrode lithium-ion battery discharge simulations: incorporating lithiation-dependent electronic conductivity and lithiation gradient due to charge cycle, J. Electrochem. Soc. 167 (2020), 140542, https://doi.org/10.1149/1945-7111/abc747.
[9] K.G. Gallagher, S.E. Trask, C. Bauer, T. Woehrle, S.F. Lux, M. Tschech, P. Lamp, B. J. Polzin, S. Ha, B. Long, Q. Wu, W. Lu, D.W. Dees, A.N. Jansen, Optimizing areal capacities through understanding the limitations of lithium-ion electrodes, J. Electrochem. Soc. 163 (2016) A138–A149, https://doi.org/10.1149/2.0321602jes.
[10] M. Ebner, D.W. Chung, R.E. Garcia, V. Wood, Tortuosity anisotropy in lithium-ion battery electrodes, Adv. Energy Mater. 4 (2014) 1–6, https://doi.org/10.1002/aenm.201301278.
[11] A. Mistry, S. Trask, A. Dunlop, G. Jeka, B. Polzin, P.P. Mukherjee, V. Srinivasan, Quantifying negative effects of carbon-binder networks from electrochemical performance of porous Li-ion electrodes, J. Electrochem. Soc. 168 (2021), 070536, https://doi.org/10.1149/1945-7111/ac1033.
[12] R. Elango, A. Nadeina, F. Cadiou, V. De Andrade, A. Demortière, M. Morcrette, V. Seznec, Impact of electrode porosity architecture on electrochemical performances of 1 mm-thick LiFePO4 binder-free Li-ion electrodes fabricated by spark plasma sintering, J. Power Sources 488 (2021), 229402, https://doi.org/10.1016/j.jpowsour.2020.229402.
[13] J. Li, T. Zhang, C. Han, H. Li, R. Shi, J. Tong, B. Li, Crystallized lithium titanate nanosheets prepared: via spark plasma sintering for ultra-high rate lithium ion batteries, J. Mater. Chem. A 7 (2019) 455–460, https://doi.org/10.1039/c8ta10680k.
[14] J. Park, C. Jeon, W. Kim, S.J. Bong, S. Jeong, H.J. Kim, Challenges, laser processing and electrochemical characteristics on application of ultra-thick electrode for high-energy lithium-ion battery, J. Power Sources 482 (2021), 228948, https://doi.org/10.1016/j.jpowsour.2020.228948.
[15] J. Neuhaus, E. von Harbou, H. Hasse, Physico-chemical properties of solutions of lithium bis(fluorosulfonyl)imide (LiFSI) in dimethyl carbonate, ethylene carbonate, and propylene carbonate, J. Power Sources 394 (2018) 148–159, https://doi.org/10.1016/j.jpowsour.2018.05.038.
[16] J. Neuhaus, D. Bellaire, M. Kohns, E. von Harbou, H. Hasse, Self-diffusion coefficients in solutions of lithium bis(fluorosulfonyl)imide with dimethyl carbonate and ethylene carbonate, Chemie-Ingenieur-Technik 91 (2019) 1633–1639, https://doi.org/10.1002/cite.201900040.
[17] L. Li, S. Zhou, H. Han, H. Li, J. Nie, M. Armand, Z. Zhou, X. Huang, Transport and electrochemical properties and spectral features of non-aqueous electrolytes containing LiFSI in linear carbonate solvents, J. Electrochem. Soc. 158 (2011) A74, https://doi.org/10.1149/1.3514705.
[18] Z. Nie, R. Parai, C. Cai, C. Michaelis, J.M. LaManna, D.S. Hussey, D.L. Jacobson, D. Ghosh, G.M. Koenig, Pore microstructure impacts on lithium ion transport and rate capability of thick sintered electrodes, J. Electrochem. Soc. 168 (2021), 060550, https://doi.org/10.1149/1945-7111/ac0bf6.
[19] Z. Nie, R. Parai, C. Cai, D. Ghosh, G.M. Koenig, Improving high rate cycling limitations of thick sintered battery electrodes by mitigating molecular transport limitations through modifying electrode microstructure and electrolyte conductivity, Mol. Syst. Des. Eng. 6 (2021) 708–712, https://doi.org/10.1039/d1me00082a.
[20] C. Cai, H. Dong, G.M. Koenig, Anisotropic particle synthesis and characterization for lithium-ion battery electrode materials via precursor precipitate growth inhibitor, Powder Technol. 394 (2021) 214–224, https://doi.org/10.1016/j.powtec.2021.08.060.
[21] Y.H. Lee, J.S. Kim, J. Noh, I. Lee, H.J. Kim, S. Choi, J. Seo, S. Jeon, T.S. Kim, J. Y. Lee, J.W. Choi, Wearable textile battery rechargeable by solar energy, Nano Lett. 13 (2013) 5753–5761, https://doi.org/10.1021/nl403860k.
[22] L. Kuang, T. Zhu, K. Li, J. Daniels, P. Herrero, P. Georgiou, Live demonstration: an IoT wearable device for real-time blood glucose prediction with edge AI, in: BioCAS 2021 - IEEE Biomed. Circuits Syst. Conf. Proc 7281, 2021, https://doi.org/10.1109/BioCAS49922.2021.9644975.
[23] M. Doyle, Comparison of modeling predictions with experimental data from plastic lithium ion cells, J. Electrochem. Soc. 143 (1996) 1890, https://doi.org/10.1149/1.1836921.
[24] T.F. Fuller, Simulation and optimization of the dual lithium ion insertion cell, J. Electrochem. Soc. 141 (1994) 1, https://doi.org/10.1149/1.2054684.
[25] J. Xie, N. Imanishi, T. Matsumura, A. Hirano, Y. Takeda, O. Yamamoto, Orientation dependence of Li-ion diffusion kinetics in LiCoO2 thin films prepared by RF magnetron sputtering, Solid State Ionics 179 (2008) 362–370, https://doi.org/10.1016/j.ssi.2008.02.051.
[26] K. Zaghib, M. Simoneau, M. Armand, M. Gauthier, Electrochemical study of Li4Ti5O12 as negative electrode for Li-ion polymer rechargeable batteries, J. Power Sources 81–82 (1999) 300–305, https://doi.org/10.1016/S0378-7753(99)00209-8.
[27] Z. Qi, G.M. Koenig, High-performance LiCoO2 sub-micrometer materials from scalable microparticle template processing, ChemistrySelect 1 (2016) 3992–3999, https://doi.org/10.1002/slct.201600872.
[28] Z. Qi, G.M. Koenig, A carbon-free lithium-ion solid dispersion redox couple with low viscosity for redox flow batteries, J. Power Sources 323 (2016) 97–106, https://doi.org/10.1016/j.jpowsour.2016.05.033.
[29] B.T. Habte, F. Jiang, Microstructure reconstruction and impedance spectroscopy study of LiCoO2, LiMn2O4 and LiFePO4 Li-ion battery cathodes, Microporous Mesoporous Mater. 268 (2018) 69–76, https://doi.org/10.1016/j.micromeso.2018.04.001.
[30] J. Chen, L. Yang, S. Fang, S.I. Hirano, K. Tachibana, Synthesis of hierarchical mesoporous nest-like Li4Ti5O12 for high-rate lithium ion batteries, J. Power Sources 200 (2012) 59–66, https://doi.org/10.1016/j.jpowsour.2011.10.052.
[31] J. Mao, W. Tiedemann, J. Newman, Simulation of Li-ion cells by dualfoil model under constant-resistance load, ECS Trans. 58 (2014) 71–81, https://doi.org/10.1149/05848.0071ecst.
[32] K. Kataoka, Y. Takahashi, N. Kijima, J. Akimoto, K.ichi Ohshima, Single crystal growth and structure refinement of Li4Ti5O12, J. Phys. Chem. Solids 69 (2008) 1454–1456, https://doi.org/10.1016/j.jpcs.2007.10.134.
[33] N. Nitta, F. Wu, J.T. Lee, G. Yushin, Li-ion battery materials: present and future, Mater. Today 18 (2015) 252–264, https://doi.org/10.1016/j.mattod.2014.10.040.
[34] S. Levasseur, M. Ménétrier, E. Suard, C. Delmas, Evidence for structural defects in non-stoichiometric HT-LiCoO2: electrochemical, electronic properties and 7Li NMR studies, Solid State Ionics 128 (2000) 11–24, https://doi.org/10.1016/S0167-2738(99)00335-5.
[35] I. Saadoune, C. Delmas, 39. The insulator – metal transition upon lithium deintercalation from LiCoO2: electronic properties and 7Li NMR study, J. Mater. Chem. 9 (1999) 1135–1140, https://doi.org/10.1039/A900016J.
[36] C. Cai, Z. Nie, G.M. Koenig, Multicomponent two-layered cathode for thick sintered lithium-ion batteries, Mater. Adv. (2022), https://doi.org/10.1039/d1ma01074c.
[37] D. Young, A. Ransil, R. Amin, Z. Li, Y.M. Chiang, Electronic conductivity in the Li4/3Ti5/3O4-Li7/3Ti5/3O4 system and variation with state-of-charge as a Li battery anode, Adv. Energy Mater. 3 (2013) 1125–1129, https://doi.org/10.1002/aenm.201300134.
[38] C. Capiglia, Y. Saito, H. Kageyama, P. Mustarelli, T. Iwamoto, T. Tabuchi, H. Tukamoto, 7Li and 19F diffusion coefficients and thermal properties of non-aqueous electrolyte solutions for rechargeable lithium batteries, J. Power Sources 81–82 (1999) 859–862, https://doi.org/10.1016/S0378-7753(98)00237-7.
[39] A. Nyman, M. Behm, G. Lindbergh, Electrochemical characterisation and modelling of the mass transport phenomena in LiPF6-EC-EMC electrolyte, Electrochim. Acta 53 (2008) 6356–6365, https://doi.org/10.1016/j.electacta.2008.04.023.
[40] J. Landesfeind, J. Hattendorff, A. Ehrl, W.A. Wall, H.A. Gasteiger, Tortuosity determination of battery electrodes and separators by impedance spectroscopy, J. Electrochem. Soc. 163 (2016) A1373–A1387, https://doi.org/10.1149/2.1141607jes.
[41] D.E. Johnson, J.R. Johnson, J.L. Hilburn, P.D. Scott, Electric Circuit Analysis, Prentice-Hall, Inc., 1997.
[42] G. Kirchhoff, Ueber die Auflösung der Gleichungen, auf welche man bei der Untersuchung der linearen Vertheilung galvanischer Ströme geführt wird, Ann. Phys. 148 (1847) 497–508.
[43] F. Pouraghajan, H. Knight, M. Wray, B. Mazzeo, R. Subbaraman, J. Christensen, D. Wheeler, Quantifying tortuosity of porous Li-ion battery electrodes: comparing polarization-interrupt and blocking-electrolyte methods, J. Electrochem. Soc. 165 (2018) A2644–A2653, https://doi.org/10.1149/2.0611811jes.
[44] N. Ogihara, S. Kawauchi, C. Okuda, Y. Itou, Y. Takeuchi, Y. Ukyo, Theoretical and experimental analysis of porous electrodes for lithium-ion batteries by electrochemical impedance spectroscopy using a symmetric cell, J. Electrochem. Soc. 159 (2012) A1034–A1039, https://doi.org/10.1149/2.057207jes.

[45] R. Morasch, J. Keilhofer, H.A. Gasteiger, B. Suthar, Methods—understanding porous electrode impedance and the implications for the impedance analysis of Li-ion battery electrodes, J. Electrochem. Soc. 168 (2021), 080519, https://doi.org/10.1149/1945-7111/ac1892.

[46] Z. E, H. Guo, G. Yan, J. Wang, R. Feng, Z. Wang, X. Li, Evolution of the morphology, structural and thermal stability of LiCoO2 during overcharge, J. Energy Chem. 55 (2021) 524–532, https://doi.org/10.1016/j.jechem.2020.06.071.

[47] P. Pang, Z. Wang, X. Tan, Y. Deng, J. Nan, Z. Xing, H. Li, LiCoO2@LiNi0.45Al0.05Mn0.5O2 as high-voltage lithium-ion battery cathode materials with improved cycling performance and thermal stability, Electrochim. Acta 327 (2019), 135018, https://doi.org/10.1016/j.electacta.2019.135018.

[48] B.J. Hwang, C.Y. Chen, M.Y. Cheng, R. Santhanam, K. Ragavendran, Mechanism study of enhanced electrochemical performance of ZrO2-coated LiCoO2 in high voltage region, J. Power Sources 195 (2010) 4255–4265, https://doi.org/10.1016/j.jpowsour.2010.01.040.

[49] P. Pang, P. Pang, Z. Wang, Y. Deng, J. Nan, Z. Xing, H. Li, Delayed phase transition and improved cycling/thermal stability by spinel LiNi0.5Mn1.5O4Modification for LiCoO2 cathode at high voltages, ACS Appl.Mater. Interfaces 12 (2020) 27339–27349, https://doi.org/10.1021/acsami.0c02459.

[50] X. Wang, Q. Wu, S. Li, Z. Tong, D. Wang, H.L. Zhuang, X. Wang, Y. Lu, Lithium-aluminum-phosphate coating enables stable 4.6 V cycling performance of LiCoO2 at room temperature and beyond, Energy Storage Mater. 37 (2021) 67–76, https://doi.org/10.1016/j.ensm.2021.01.031.

[51] B. Wen, Z. Deng, P.C. Tsai, Z.W. Lebens-Higgins, L.F.J. Piper, S.P. Ong, Y. M. Chiang, Ultrafast ion transport at a cathode–electrolyte interface and its strong dependence on salt solvation, Nat. Energy 5 (2020) 578–586, https://doi.org/10.1038/s41560-020-0647-0.

[52] T.F. Fuller, M. Doyle, J. Newman, Relaxation phenomena in lithium-ion-insertion cells, J. Electrochem. Soc. 141 (1994) 982.

[53] A.N. Mistry, K. Smith, P.P. Mukherjee, Secondary-phase stochastics in lithium-ion battery electrodes, ACS Appl. Mater. Interfaces 10 (2018) 6317–6326, https://doi.org/10.1021/acsami.7b17771.

[54] M. Doyle, T.F. Fuller, J. Newman, Modeling of galvanostatic charge and discharge of the lithium/polymer/insertion cell, J. Electrochem. Soc. 140 (1993) 1526–1533, https://doi.org/10.1149/1.2221597.

[55] E. Martinez-Rosas, R. Vasquez-Medrano, A. Flores-Tlacuahuac, Modeling and simulation of lithium-ion batteries, Comput. Chem. Eng. 35 (2011) 1937–1948, https://doi.org/10.1016/j.compchemeng.2011.05.007.

[56] D.Y. Wang, A. Xiao, L. Wells, J.R. Dahn, Effect of mixtures of lithium hexafluorophosphate (LiPF 6) and lithium bis(fluorosulfonyl)imide (LiFSI) as salts in Li[Ni1/3Mn1/3Co1/3]O2/graphite pouch cells, J. Electrochem. Soc. 162 (2015) A169–A175, https://doi.org/10.1149/2.0821501jes.